Prospects for engineering thermoelectric properties in $La_{1/3}NbO_3$ ceramics revealed *via* atomic-level characterization and modelling

Demie Kepaptsoglou[1*], Jakub D. Baran[2], Feridoon Azough[3], Dursun Ekren[3], Deepanshu Srivastava[3], Marco Molinari[2,4], Stephen C. Parker[2*], Quentin M. Ramasse[1] and Robert Freer[3]

*Corresponding authors: dmkepap@superstem.org, s.c.parker@bath.ac.uk

[1] SuperSTEM Laboratory, SciTech Daresbury Campus, Daresbury WA4 4AD, U.K.

[2] Department of Chemistry, University of Bath, Claverton Down, Bath BA2 7AY, U.K.

[3] School of Materials, University of Manchester, Manchester, M13 9PL, U.K.

[4] Department of Chemistry, University of Huddersfield, Huddersfield, HD1 3DH, U.K.

Abstract

A combination of experimental and computational techniques has been employed to explore the crystal structure and thermoelectric properties of A-site deficient perovskite $La_{1/3}NbO_3$ ceramics. Crystallographic data from X-ray and electron diffraction confirmed that the room temperature structure is orthorhombic with *Cmmm* as a space group. Atomically resolved imaging and analysis showed that there are two distinct A-sites: one is occupied with La and vacancies and the second site is fully un-occupied; the diffuse super-structure reflections observed through diffraction techniques are shown to originate from La vacancy ordering. $La_{1/3}NbO_3$ ceramics sintered in air showed promising high temperature thermoelectric properties with a high Seebeck coefficient of S_1 = -650 to -700 µV/K and a low and temperature-stable thermal conductivity of k = 2 to 2.2 W/mK in the temperature range of 300 to1000 K. First-principles electronic structure calculations are used to link the temperature dependence of the Seebeck coefficient measured experimentally to the evolution of the density of states with temperature and indicate possible avenues for its further optimization through electron doping and control of the A-site occupancies. Moreover, lattice thermal conductivity calculations give an insight into the dependence of the thermal conductivity on specific crystallographic directions of the material, which could be exploited *via* nano-structuring to create high-efficiency compound thermoelectrics.

Keywords: Thermoelectric oxides, crystal structure, DFT, electronic structure, STEM, EELS

1. Introduction

There are limited numbers of ceramic compositions suitable for high temperature thermoelectric (TE) applications.[1] The most promising candidates include $SrTiO_3$-based perovskites[2], zinc oxide, tungsten bronze compositions and homologous compounds.[3,4] Among these candidates, $SrTiO_3$ (STO) is one of the most promising high temperature n-type oxide thermoelectrics[5], as it has a high Seebeck coefficient[6] and a simple perovskite structure which easily lends itself to doping and thus to tailoring of its electron and thermal transport properties.[7–9] However, one of the drawbacks of $SrTiO_3$-based ceramics is their high thermal conductivity with strong temperature dependence (from 10 W/K m at ambient temperature to 4 W/K m at 1000 K).[1]

Therefore, in the search for new oxides with low thermal conductivities, which could be used on their own as new materials or in conjunction with STO as binary systems[7], we have identified A-site deficient perovskites as systems with great potential in thermoelectric applications.[7,10–12] Of particular interest, $La_{1/3}NbO_3$ (hereafter denoted LNO) is a leading contender as its vacancy content in the lattice, the highest among the A-site deficient perovskite family (whereby 2/3 of the A-sites are vacant), may promote glass-like low thermal conductivity[13]. The constituent cations of LNO, namely La and Nb, have been previously used as A- and B- site dopants respectively in $SrTiO_3$ (separately or as co-dopants),[14–19] in order to achieve improved thermoelectric properties. This shared chemistry thus provides a direct pathway to integration with STO in a binary system.

In this work we investigate the microstructural and electronic properties of the A-site deficient LNO ceramic itself, by applying a range of selected experimental and computational techniques, and we report for the first time promising thermoelectric properties.

The complex balance between the chemistry, microstructure and the electronic structure of a material determines macroscopic quantities such as the electrical conductivity σ, the Seebeck coefficient S or the thermal conductivity κ, which when expressed *via* the dimensionless figure of merit $ZT = \frac{\sigma S^2}{\kappa} T$ at a given temperature T, determine the efficiency of materials for practical TE applications. A thorough characterisation at the atomic scale of LNO's structure and chemistry is therefore essential to understand its macroscopic properties. Here we use aberration-corrected scanning transmission electron microscopy (STEM) and electron energy loss spectroscopy (EELS) to validate at the atomic scale and along several zone axes the structure of LNO, to

support results from bulk characterisation techniques such as X-ray diffraction. This atomic scale view allows us to determine precisely the cation distribution in the structure, which has an important impact on the macroscopic properties of the ceramic. The electronic transport properties are indeed directly related to the topology of the electronic states near the Fermi energy (E_F). Density functional theory electronic band-structure calculations combined with the Boltzmann transport theory[20], informed by our structural and chemical characterisation, are therefore used to explain with excellent agreement the origin of promising electronic thermoelectric properties we measure experimentally, especially at high temperatures. A large-scale-potential model-based molecular dynamics approach is then used to include LNO's microstructure into the simulations and to evaluate its impact on the thermal transport properties.

This combined theoretical and experimental approach provides the most complete description to date of the crystallographic and electronic structure of LNO as well as of its thermoelectric properties. Furthermore, the *ab initio* simulations allow us to make predictions about how LNO's thermoelectric properties change as a function of electron doping concentration, which our STEM-EELS atomic-scale characterisation suggests can be readily influenced by modifying the local structure of the material. These results therefore offer a pathway to nanostructuring LNO, possibly through synthesis and/or processing, into a promising and efficient thermoelectric material.

2. Methods

2.1. Experimental details

Ceramic samples of LNO were prepared by the conventional mixed oxide route. Starting materials were high purity powders of La_2O_3 (Solvay, 99.95%) and of Nb_2O_5 (Solvay, 99.5%). The powders were weighed in batches according to the required formulations and wet milled for 24 hours in a vibratory mill using zirconia balls and propan-2-ol. The powders were then dried at 85 ^oC for 24 hours and calcined at 1100 ^oC for 4 hours. The calcined powders were again wet-milled for 24 hours in a vibratory mill using zirconia balls and propan-2-ol. Powders were then uniaxially compacted into pellets of 20 mm diameter and 5 mm thickness at a pressure of

50 MPa prior to sintering at 1300-1350^{o}C for 4 hours in air on a platinum substrate. A cooling rate of 180 ^{o}C/hr was used.

Densification was assessed by the Archimedes method. Structural analysis was undertaken by X-ray diffraction using a Philips PW1830 system operating at 50 kV and 40 mA. The samples were first ground flat using 400 grade SiC and then scanned from 10^{o}-100 ^{o} 2θ in steps of 0.05^{o} with a dwell time of 20 s per step. Rietveld analysis of the data was undertaken using TOPAS 4.2.[11] Microstructures were examined by scanning electron microscopy using a Philips XL30 FEG-SEM equipped with EDX capability.

Samples for electron microscopy investigations were prepared by conventional crushing (pestle and mortar) techniques. The crushed powders were dispersed in chloroform, drop cast onto a copper grid covered with a holey carbon support film, and then dried. The specimen structures were initially investigated using selected area electron diffraction (SAED) and high-resolution transmission electron microscopy (HRTEM) techniques using a FEI FEG-TEM (Tecnai G2, Hillsboro, OR) operated at 300 kV. Subsequently, atomic-resolution structural characterization was carried out using an aberration-corrected dedicated scanning transmission electron microscope (STEM) (UltraSTEM^{TM}100) which is equipped with a Gatan Enfina electron energy loss spectrometer. This microscope was operated at 100 kV acceleration voltage and the probe-forming optics were adjusted to form a 0.9 Å electron probe with a convergence of 31 mrad and beam current of approximately 75 pA. The high-angle annular-dark-field (HAADF) detector inner and outer semi-angles were calibrated at 82-189 mrad, while for all electron energy loss spectroscopy (EELS) data presented here the collection semi-angle (spectrometer acceptance angle) was 36 mrad. Additional EELS measurements at high energy resolution were performed using the Nion UltraSTEM 100MC-'HERMES' dedicated STEM[21], which is equipped with an electron monochromator and a Gatan Enfinium spectrometer. The microscope was operated at 60 kV and the monochromator and probe forming optics were adjusted to provide a beam energy spread of 0.025 eV, whilst retaining a 0.9 Å electron probe size, with a convergence of 30 mrad and beam current of approximately 20 pA after monochromation. The EELS acceptance angle was 46 mrad.

The chemical maps presented in this work were acquired using the spectrum imaging (SI) technique, whereby the electron probe is rastered serially across a defined area of the specimen

(such as those marked by yellow rectangles in Figures 4 and 5), recording an EEL spectrum at each position. EELS SI for chemical mapping were de-noised by Principal Component Analysis using the MSA Cime- EPFL plugin[22] for Digital Micrograph. Chemical maps were subsequently produced by integrating pixel-by-pixel the intensity of the relevant element ionisation edge (in this instance the Nb $L_{2,3}$ and La $M_{4,5}$ edges) over a fixed energy window of 30 eV above its onset, after subtraction of the decaying background using a standard power law fitting function.

Stacks of rapidly-acquired HAADF STEM frames, were corrected for specimen drift and scanning distortions using non-rigid registration techniques[23] as implemented in the commercially-available Smart Align Plugin.[24] The images were further corrected for orthogonality using the Jitterbug plugin[25,26].

Dynamic SAED simulations were performed using the JEMS simulation software[27]. Multi-slice image simulations of HAADF STEM images were performed using the Dr.Probe[28] simulation package. The parameters used for SAED and image simulations (e.g. acceleration voltage, aberration coefficients, acceptance angles, specimen thickness, etc.) reflect the exact experimental conditions under which the LNO ceramic was observed. The structural parameters for the simulations were taken from Ref.[29]

The Seebeck coefficient and electrical conductivity were measured simultaneously using a ULVAC ZEM 3 in helium atmosphere. Thermal conductivity was obtained by measuring the density (Archimedes method), thermal diffusivity (using a custom-built apparatus in argon atmosphere) and heat capacity (Netzsch STA 449C; nitrogen atmosphere).

2.2.Computational details

Density Functional Calculations

First-principles density functional theory calculations within the framework of the plane-wave projector augmented wave formalism,[30] as implemented in Vienna *ab initio* simulation package (VASP) [31–33] have been carried out in order to calculate the ground state atomic and electronic structure of LNO. The exchange correlation functional used for these calculations was PBE[34] with the inclusion of the Hubbard *U* term (PBE+*U*) within the Dudarev *et al.* approach.[35] The selected value of U_{eff} was 4 eV to treat the Nb *4d* electrons. The PBE+*U* methodology introduces an energy penalty for non-localized states that improves the localization of *d*-electrons. The

plane-wave cut-off energy was 500 eV and the Monkhorst-Pack *k*-mesh was 4x4x6. Electronic degrees of freedom have been converged to 10^{-7} eV, whereas the ionic degrees of freedom were converged until the forces acting on the ions became smaller than $1x10^{-2}$ eV/atom. For defect calculations, because of the partial occupancy of the A sites observed experimentally, and due to size restrictions in DFT calculations, we used a model structure for LNO with lattice parameters 8.93Å x 8.06 Å x 5.67 Å, 90.0 x 71.62 x 90.0 degrees, *i.e.* a 208 atom unit cell with k-point sampling performed at the Γ-point of the Brillouin zone. The minimum distance between periodic images of point defects is 11.15 Å with this model cell. The formation energy of a neutral oxygen vacancy, $E_f[V_O^x]$, comprising an oxygen vacancy and reduced neighbouring niobium ions that ensures charge neutrality, was determined from equation 1[36] that assumes thermodynamic equilibrium:

$$E_f[V_O^x] = E_{tot}[V_O^x] - E_{tot}[bulk] + \frac{1}{2}\mu_{O_2} \quad (1)$$

Here $E_{tot}[V_O^x]$ is the energy of the supercell containing a V_O^x, $E_{tot}[bulk]$ is the total energy of the non-defective $La_{1/3}NbO_3$, and μ_{O_2} is the chemical potential of molecular oxygen. μ_{O_2} has been calculated as the total energy of the O_2 molecule in the ground state (triplet) in vacuum in a cubic simulation cell of 28 Å. This is a standard procedure and assumes thermodynamic equilibrium with a reservoir of oxygen gas under oxygen-rich conditions and excludes thermal contributions to the chemical potential.[37]

Boltzmann Transport Calculations

The transport properties were calculated using the Boltzmann transport equation as implemented in the BoltzTraP code.[38] For this purpose Kohn-Sham eigenenergies have been calculated on a denser 24x24x28 *k*-point mesh for our model LNO structure, which results in 4032 irreducible *k*-points. The transport calculations are carried out as a function of temperature and chemical potential employing constant relaxation time (τ) approximation (CRTA), which neglects the weak energy dependence of τ but recovers some doping and temperature dependence.[38] The CRTA methodology has been successfully applied to other oxide thermoelectric materials.[39–41] Within this methodology, τ is exactly cancelled in the expression of the Seebeck coefficient, and thus can be directly evaluated from the first-principles band structure.

Molecular Dynamics for Thermal Conductivity Calculations.

To carry out thermal conductivity calculations, classical molecular dynamics (MD) simulations were performed using the LAMMPS package.[42] The system considered consists of a 50.03 x 50.03 x 33.77 Å simulation box of $La_{1/3}NbO_3$ containing 4492 atoms. The interatomic potentials developed by Teter[43] based on partially-charged rigid ions were used as listed in Table 1. Firstly, the simulation cell was relaxed in the NPT ensemble for 1 ns with a time step of 1 fs until the fluctuation of the volume was minimized at a given temperature. Secondly, further relaxation was performed in the canonical ensemble (NVT) as in the previous step. With the relaxed systems, we then carried out the thermal conductivity calculations within the Green-Kubo formalism.[44,45] The heat flux of the system was calculated under the NVT ensemble for 5 ns at intervals of 10 time steps and correlated at each time interval. The correlations were then integrated along each spatial dimension, resulting in thermal conductivities as a function of integral length, as in previous studies.[2,46]

Table 1. Teter potential parameters $\boldsymbol{A_{ij}}$, $\boldsymbol{\rho_{ij}}$ and $\boldsymbol{C_{ij}}$ used in the Buckingham equation $\boldsymbol{\varphi_{ij} = A_{ij}\exp(-r_{ij}/\rho_{ij}) - (C_{ij}/r_{ij}^6)}$ representing the interactions between ions in $La_{1/3}NbO_3$, and associated with atomic symbols partial charges.

Interactions	A_{ij} (eV)	ρ_{ij} (Å)	C_{ij} (eVÅ^6)
$La^{1.8+}$– $O^{1.2-}$	4369.3930	0.278603	60.278
$Nb^{3.0+}$– $O^{1.2-}$	11448.856	0.228482	95.193
$O^{1.2-}$– $O^{1.2-}$	1844.7458	0.343645	192.58

3. Results and Discussion

3.1. Crystal structure

X-ray diffraction

One of the earliest structural studies of $La_{1/3}NbO_3$ was carried out by Iyer *et al.*[47] The study showed that the material has an orthorhombic perovskite structure where the *c*-planes (see figure S1 in the Supplementary Information provided for a schematic representation of the crystal

structure of LNO) are preferentially occupied by La atoms. Later studies[47,48] supported this result and also suggested that ordered A-site vacancies lead to the formation of a superlattice with c≈2a. The crystal symmetry was suggested to be orthorhombic at room temperature with lattice parameters related to the parent perovskite structure as a ≈ $a_{perovskite}$, b ≈ $a_{perovskite}$, and c ≈ $2a_{perovskite}$. This was confirmed by the *in-situ* synchrotron X-ray powder diffraction study of Kennedy *et al.*[49], which also identified the room temperature space group of the compound as *Cmmm*. The structure was shown to transform to a tetragonal symmetry, *P4/mmm* with a ≈ $a_{perovskite}$, b ≈ $a_{perovskite}$, and c ≈ $2a_{perovskite}$, at 195°C, being stable up to 500°C. These structures were further supported by subsequent diffraction studies[29,50], while electron diffraction studies carried out by Garcia-Martin *et al.*[51] showed the presence of superlattice reflections in the electron diffraction patterns, indicating a doubling of the c-axis. The same study showed the presence of diffuse satellite reflections attributed to the presence of a modulated structure.

Experimental X-ray diffraction patterns of the LNO compound presented in this work are, in agreement with literature,[29,49] indexed based on the orthorhombic structure, using the *Cmmm* space group and a ≈ $2a_{perovskite}$, b ≈ $2a_{perovskite}$, and c ≈ $2a_{perovskite}$, as shown in Figure 1. The experimental X-ray data were refined using structural files available in the literature: two independently-derived structure files, namely ICSD 90692 and 150448 (corresponding to Refs[29,49], respectively), were used for completeness, yielding similar goodness of fits. The lattice parameters, fractional coordinates, site occupancies and isotropic thermal parameters are listed in Table S1 of the Supplementary Information provided.

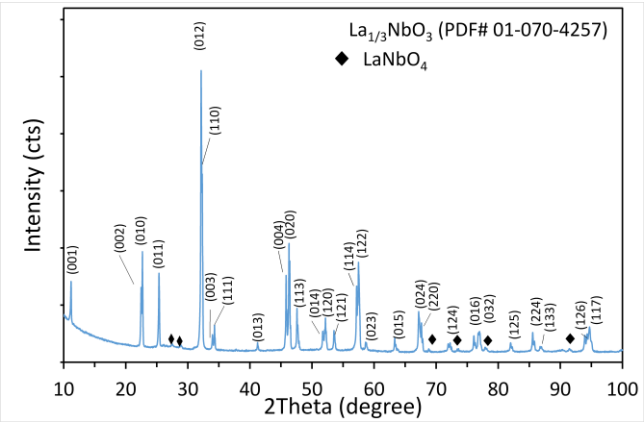

Figure 1: X-ray diffraction pattern for LNO. The diffraction peaks indicated by black diamond markers correspond to a $LaNbO_4$ minor secondary phase.

Electron Microscopy

The local atomic structure and symmetry of the LNO ceramic were further investigated by transmission electron microscopy techniques. Selected Area Electron Diffraction Patterns (SAED) acquired along two zone axis, namely [100] and [101] are shown in Figure 2a and c, respectively, alongside the corresponding simulated electron diffraction patterns (Figures 2b and 2d, respectively) using the *Cmmm* space group. The diffuse satellite reflections expected from the X-ray characterisation can be clearly seen along the $[22\bar{2}]$ direction.

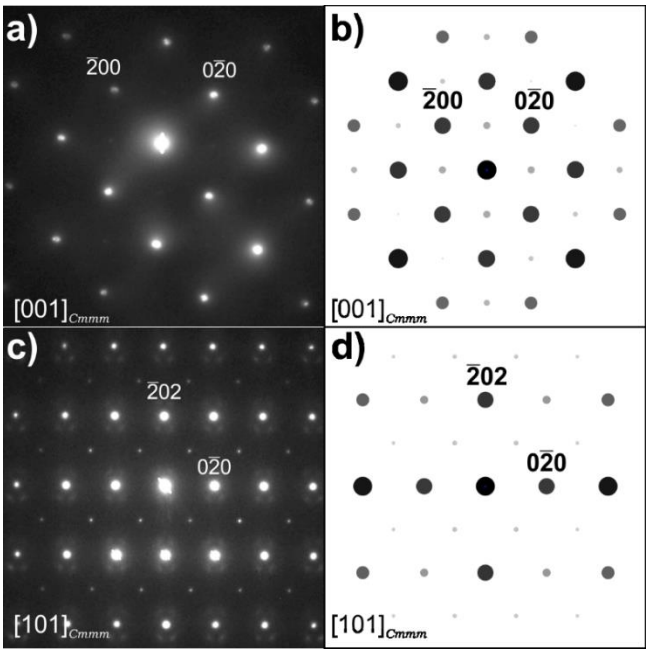

Figure 2: Experimental SAED patterns acquired along the (a) $[001]_{Cmmm}$ and c) $[101]_{Cmmm}$ zone axes, and corresponding simulated patters in panels (b) and (d), respectively. The experimental diffraction patterns only show the characteristic diffuse satellite reflections along the $[\mathbf{22\bar{2}}]$ direction.

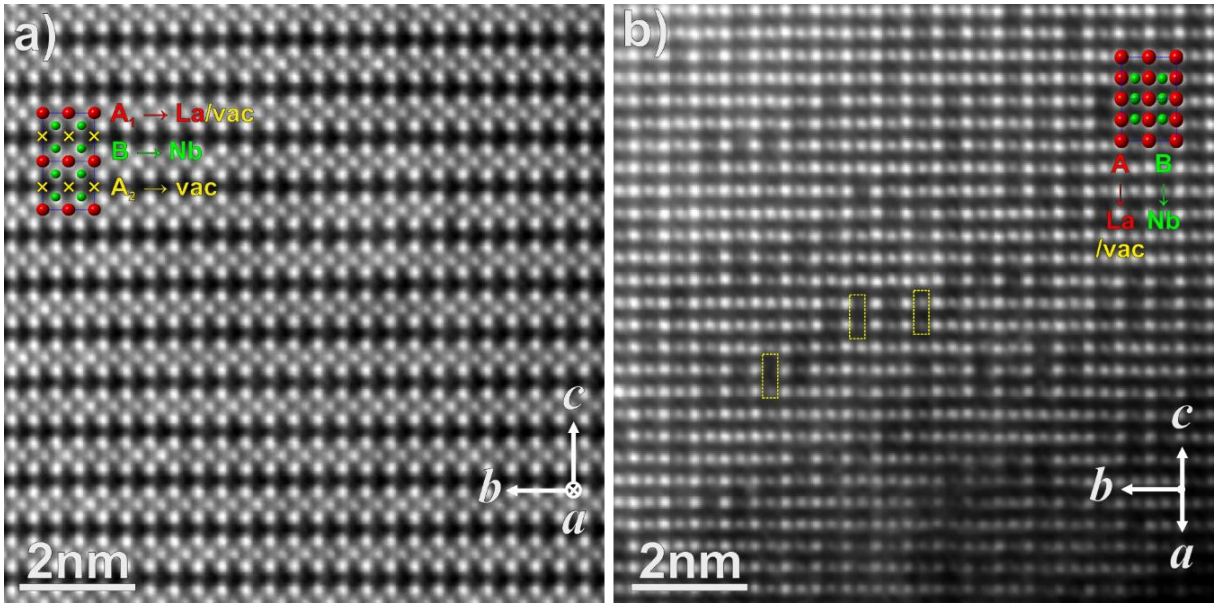

Figure 3: HAADF STEM images (averaged by non-rigid registration[23] from a stack of 50 consecutive frames) of the LNO ceramic acquired along the a) [100] and b) [101] zone axes. The corresponding ball-and-stick models of the LNO *Cmmm* structure[29] (oxygen positions not shown), are overlaid on the images for comparison (where yellow × symbols denote the vacant A_2 sites).

Atomic-scale details of the LNO structure can be observed in atomic number (Z) sensitive HAADF STEM images acquired along the [100] and [101] zone axes (Figures 3a and b, respectively); ball and stick models of the cation sites of the *Cmmm* space group are overlaid for reading clarity. In the HAADF images acquired along the [100] axis (Figure 3a) the B-site columns, occupied by Nb (Z_{Nb}=41), appear brighter than the A-site columns, occupied by the heavier La (Z_{La}=57). This apparent counter-intuitive HAADF image intensity discrepancy ($Z_{Nb}^2 = 168\ vs\ Z_{La}^2 = 3249$),[i (footnote:see end of main text)] originates from the partial occupancy of the two A-sites of the LNO perovskite structure (A_1 and A_2, respectively). When the structure is observed along the [100] axis, the two A-sites are viewed as separate columns; the A_1 site is occupied by La and vacancies in a 3:1 ratio, resulting in a lower total intensity than that of the neighbouring Nb B-sites (see also a comparison with multi-slice HAADF image simulations, in Figure S4 of the Supplementary Information provided). On the other hand, the A_2-site is fully unoccupied and thus no intensity appears at these positions in HAADF images, giving the impression of a layered structure along the *c*-axis. The layering of the crystal structure can be

further decomposed into two distinct sub-units along the *c*-axis; quantitative analysis of HAADF images obtained using a high-precision workflow reveals that the distance $c_1 \approx 3.85 \pm 0.02$ Å between B-sites on either side of the partially occupied A_1 cation layer is wider than the distance $c_2 \approx 4.23 \pm 0.02$ Å between B-sites on either side of the fully-vacant A_2 layer, with $c_1 + c_2 = 2c_{perovskite}$ (for details see Figure S3 in the Supporting Information provided). These observations are further corroborated by atomically-resolved STEM EELS chemical maps shown in Figure 4, which highlight the alternating partially-occupied La A_1 and fully vacant La A_2 sites, respectively, and confirm directly that the Nb columns are more closely spaced around the empty A_2 layer (Figure 4c and Figure S3 in the Supplementary information provided).

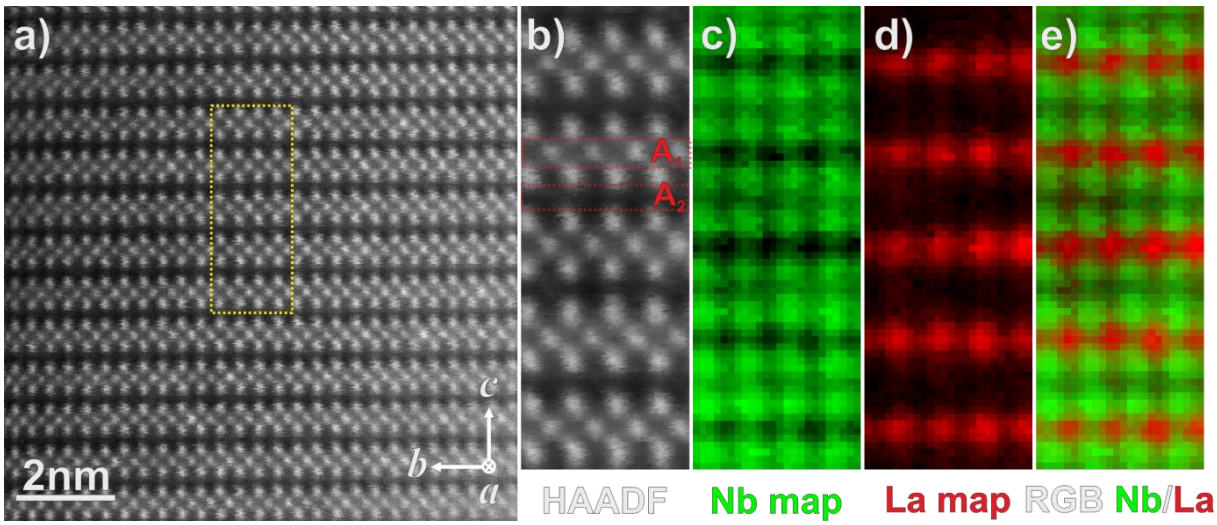

Figure 4: Example of atomically-resolved EELS measurement of the LNO ceramic, performed along the [100] zone axis: a) HAADF STEM Survey image, showing the area used for analysis marked by a yellow rectangle, b) HAADF STEM signal intensity acquired simultaneously with the EELS signal, c) integrated EELS intensity map of the Nb $L_{2,3}$ edge, d) integrated EELS intensity map of the La $M_{4,5}$ edge and e) RGB overlay of the Nb and La maps.

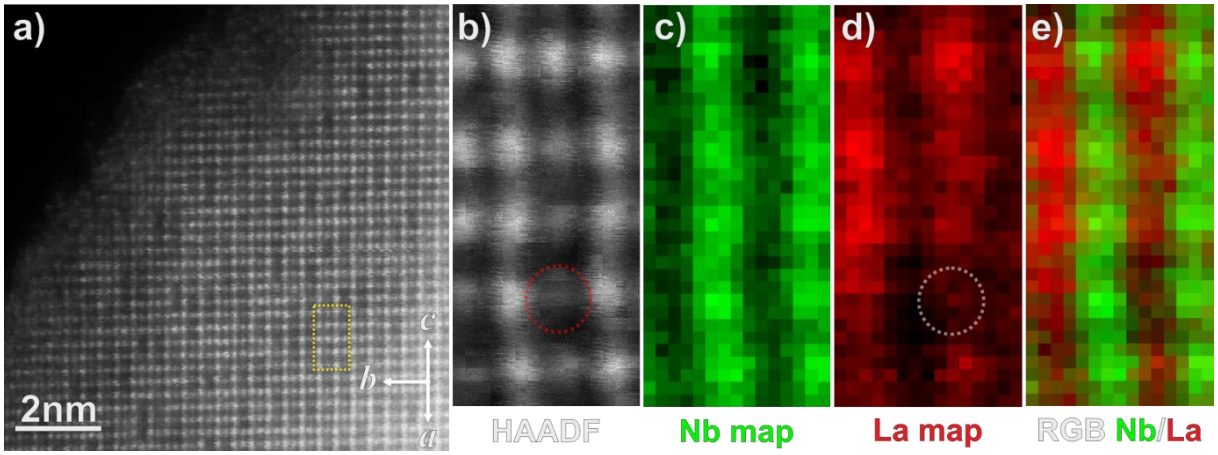

Figure 5: Example of atomically-resolved EELS measurement of the LNO ceramic, performed along the [101] zone axis: a) HAADF STEM Survey image, showing the area used for analysis marked by a yellow rectangle, b) integrated HAADF STEM signal intensity acquired simultaneously with the EELS signal, c) integrated EELS intensity map of the Nb $L_{2,3}$ edge, d) integrated EELS intensity map of the La $M_{4,5}$ edge and e) RGB overlay of the Nb and La maps.

In HAADF STEM images acquired along the [101] zone axis (Figure 3b and image simulations in Figure S4 in the Supplementary Information provided), the intensity of the B-site columns also appears brighter than that of the A-site (in this projection, the A_1 and A_2 sites overlap), again due to the high vacancy content of the La columns. Furthermore, and upon closer inspection of the atomic-resolution HAADF images in the [101] zone axis, the distribution of the high-vacancy content A-site columns appears to be locally non-uniform. Dark columns can often be observed to be grouped in adjacent pairs (Figure 3b and Figure S5 in the Supplementary Information provided). This implies that the A_1-site vacancies are not uniformly distributed across this layer (as the A_2-site is fully unoccupied). Interestingly, the high vacancy column pairs appear to be lying in lines parallel to the $[\bar{1}11]$ and $[11\bar{1}]$ directions (see also Figure S5 in the Supplementary Information provided). It is this pairing which gives rise to the satellite reflections observed across the $[22\bar{2}]$ reflections in the [101] SAED patterns (Figure 2b here and Ref.[52]) due to A_1 vacancy ordering along those planes. Atomic-resolution EELS maps in the [101] orientation corroborate these conclusions: a lower La signal intensity is systematically observed at positions corresponding to darker atomic columns in the simultaneously acquired HAADF images (Figure 5).

The presence of cation vacancy ordering and clustering in LNO is of particular interest for its potential application as TE oxide and particularly to understand thermal conductivity. In addition to the intrinsic layered nature of the structure of LNO, which is desirable for thermal transport properties, the observed cation vacancy ordering has further potential for suppressing thermal conductivity. Extensive studies on A-site deficient perovskite systems [10–12,53–56] show that that cation vacancy-ordering in these systems is associated with the presence of oxygen octahedral nano-domains and localised oxygen octahedral distortions.[11,53,57] Such nanostructuring can be used to promote glass-like thermal conductivity[13,58] while the clustering of cation vacancies can induce rattling modes, suppressing further thermal conductivity in layered systems.[59] These intriguing structural features therefore point to a possible application of LNO as a promising thermoelectric material, and we therefore investigated its transport properties both experimentally and using *ab initio* simulations.

3.2 Electronic and Thermal Transport Properties

There is only limited experimental data published to date on the transport properties of LNO. For instance electrical conductivity data can be found in the work of George *et al.*,[60] while to the authors' knowledge no experimental measurements of the Seebeck coefficient has been published. Thus to assess the prospects of utilizing LNO based ceramics as thermoelectric materials, thermoelectric transport properties have been measured. The experimentally determined Seebeck coefficient for the air-sintered LNO ceramic is shown in Figure 6a; the negative values observed suggest n-type behaviour. An increase in the absolute value of the Seebeck coefficient can be observed at a temperature of approximately ~480 K, where it is reaching its maximum value of ~701 μV/K, followed by a slight decrease as the temperature rises. This large value of LNO's Seebeck coefficient is directly comparable with that of other known thermoelectric oxide systems with similar behaviour: for instance $SrTiO_3$: ~1200 μV/K,[7] ZnO ~ -300 μV/K,[61] and $CaMnO_3$ ~ -200 μV/K,[46,62] respectively. Interestingly, the change in the values of Seebeck coefficient observed at ~480 K coincides with the transition from the orthorhombic to tetragonal structure.[49] Such a behaviour, observed previously in several oxide systems[63–65] raises the possibility of a connection between the two phenomena, through the occurrence, e.g., of a phonon instability.[66,67]

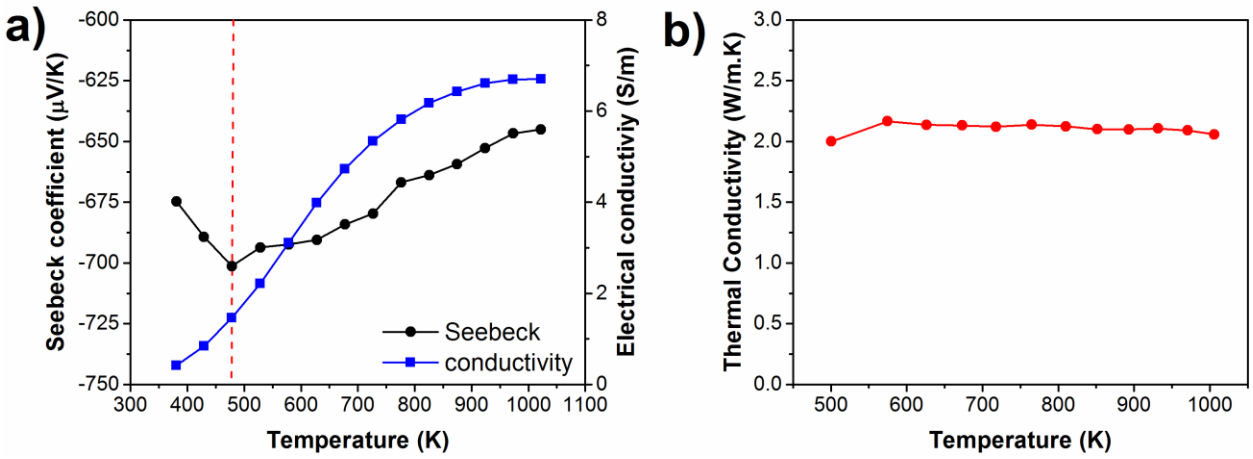

Figure 6: Experimental thermoelectric properties of LNO as a function of temperature. a) Measured Seebeck coefficient and electrical conductivity; the red line indicates the temperature for which the Seebeck coefficient has the highest value; b) Experimentally determined lattice thermal conductivity.

A clear drawback of the air-sintered LNO ceramic is its low electrical conductivity (Figure 6a), which nevertheless exhibits an increase with temperature, ranging from 0.5 to 6.7 S/m in the 300-1000 K temperature range. The low electrical conductivity results in a low figure of merit ZT (0.0013 at 1000 K). However, the electrical conductivity of LNO is higher in the same range of temperature than other thermoelectric oxides prepared in similar conditions: 12 S/m for $CaMnO_3$[62], 0.6×10^{-6} S/m for ZnO[61], and 1×10^{-7} S/m for $SrTiO_3$[15]. This motivates devising strategies for improving its transport properties, especially as LNO shows an inherently low and temperature-stable phonon glass-like thermal conductivity of ~2.1 W/mK (Figure 6b), which is highly desirable for TE applications. Higher electrical conductivity could potentially be achieved by carefully tailoring the composition and or microstructure of the material. For instance, electron doping could be achieved *via* reducing the valence of Nb, by employing a thermal treatment in reducing atmosphere, an approach similar to that used for other Nb containing TE oxides[15,64] or by doping LNO with other elements or compounds. The partial substitution of both A and B sites with elements of different valance state, for instance Ca and Sr for the A- site and Ti and Mo for the B-site, respectively, could be a viable strategy for improving the electron transport. In order to understand the underlying mechanisms of the transport properties of the

LNO system and further explore the possibility of enhancing its electrical conductivity, we have performed detailed *ab initio* calculations presented in the following section of this paper.

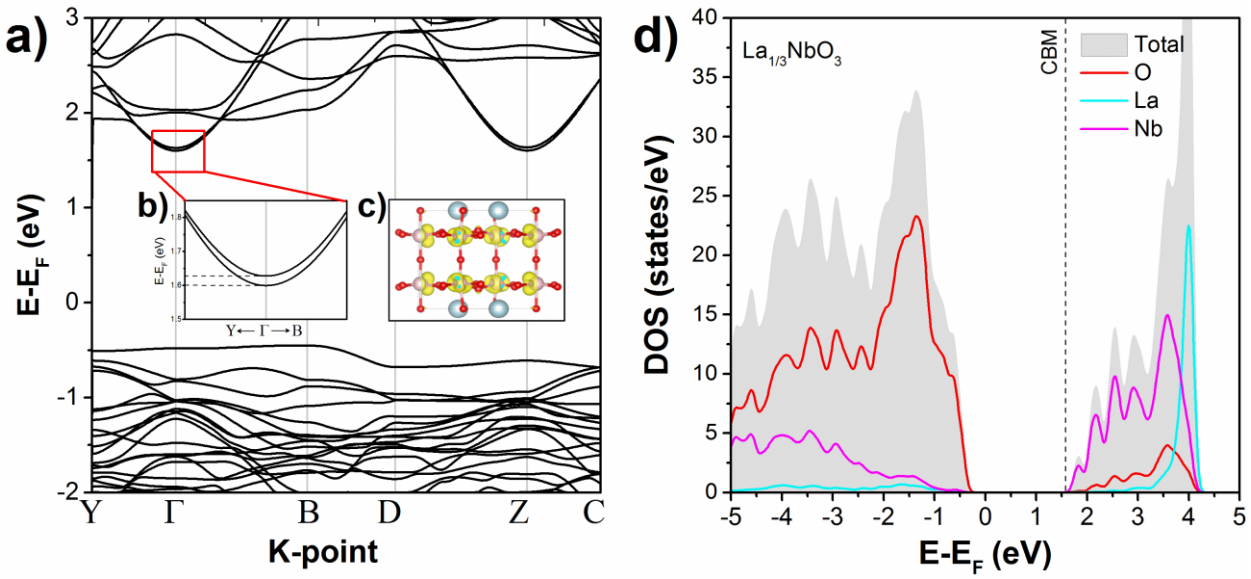

Figure 7: a) PBE+*U* band structure along the symmetry directions of the Brillouin zone. The high symmetry k-points of the primitive cell are: *Y* (½, 0, 0), Γ (0, 0, 0), *B* (0, 0, ½), *D* (0, ½, ½), *Z* (0, ½, 0) and *C* (½, ½, 0). b) Conduction bands in the vicinity of Γ. c) Charge density plot of the lowest conduction band. d) Total density and projected density of states of LNO. The CBM is indicated by the dashed lines.

3.3. Computational Results

Electronic structure calculations

One of the main features that determine the transport properties of an *n*-type semiconductor is the curvature and multiplicity of electronic bands near the conduction band minimum (CBM).[10] In general, it is desirable for good TE performance when a system possesses two or more bands near the bottom of the CBM. This higher energy degeneracy is thought to promote enhanced Seebeck coefficient as the thermopower is related to the entropy of the charge.[20] In order to gain insights into the electronic properties of LNO we calculated the band structure and density of states (DOS) of LNO as shown in Figure 7. It should be noted that the theoretical model was validated by a direct comparison of the DOS calculations projected onto the relevant atomic sites with measurements of the fine structure of the EELS O *K* edge (see Figure S6 of the SI

information provided), which in a single electron approximation is directly related to the density of empty states in the structure.

An indirect band-gap of 2.22 eV (PBE+*U*) is predicted with parabolic-like bands above the CBM (Figure 7b). The band structure also reveals that in LNO the valence band maximum (VBM) is located at the B-point of the Brillouin zone, which is only 30 meV above the valence band at the Γ-point. The two CBM are at the Γ-point and Z-point (Figure 7b) that are separated (*ΔE*) by 29 and 34 meV, respectively. Figure 7d shows the total and DOS projected on the different atomic species of LNO.

The upper valance band (VB) is derived from oxygen *2p* states, whereas the lower conduction band is dominated by Nb *4d* states (Figure 7d). This makes LNO a charge transfer insulator. To test the validity of the PBE+*U* approach in describing the electronic structure of LNO, we carried out further calculations at a higher level of theory with the hybrid HSE06 functional, which is customarily employed to validate the accuracy of GGA-functional-predicted band-gap values.[68] The upper VB and lower CB DOS (the region that defines the electronic transport properties of the system) as calculated with PBE+*U* and HSE06 are compared in Figure 8.

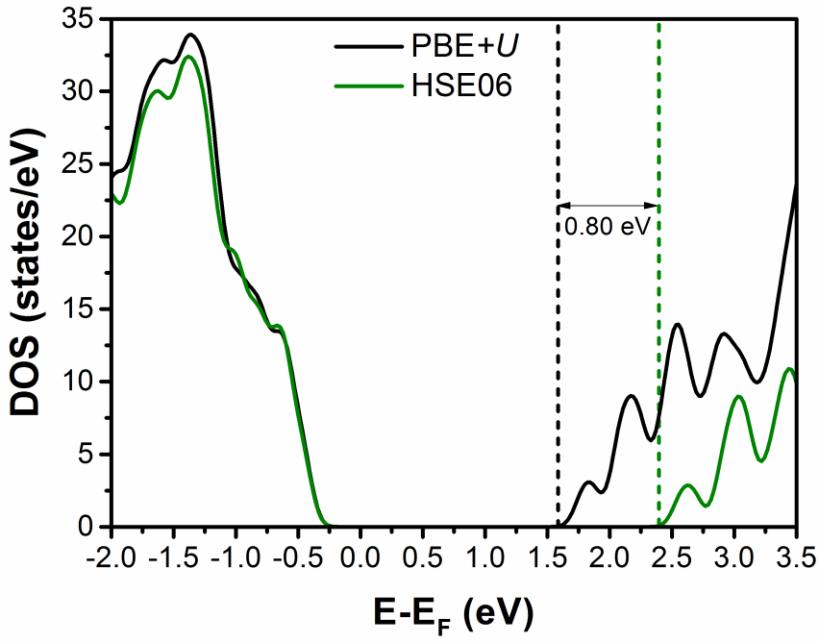

Figure 8: Total DOS of LNO as calculated with PBE+*U* and HSE06 functional.

As illustrated in Figure 8, there is almost no difference between the PBE+*U* and HSE06 DOS of the upper VB. The CB DOS is shifted by 0.80 eV towards higher energies in the case of the HSE06 functional, giving an estimated band-gap of 3.02 eV. A larger band-gap value is expected in the case of the HSE06 functional, because GGA functionals tend to underestimate the band-gap due to self-interaction errors.[69] The CB DOS nevertheless retains a very similar topology between the two methods, indicating that there is only a minor functional dependency on the calculated transport properties.

In order to further validate the theoretical approach chosen here, the band gap of LNO was measured directly with EELS using a high-energy-resolution monochromated system providing a resolution of 0.025 eV in the experimental conditions chosen here. Although an absolute match between values determined through EELS, optical techniques and theoretical simulations is often hard to reach, the measured experimental value of 3.86 eV (Supplementary Material provided) is in good agreement with the higher gap value calculated using the HSE06 functional, as well as with the optical band-gap of 3.2 eV measured by Inaguma *et al.*[70] using bulk samples. Overall, this relatively large band-gap of LNO confirmed both theoretically and experimentally ensures the absence of bipolar conduction in this system.

Ab initio thermal transport properties

Having validated the chemistry and band structure of LNO through a comparison of experiment and theory, the Seebeck coefficient (Figure 9a) can be calculated based on the application of Boltzmann transport theory (details of the calculation methodology can be found in section 2.2 of this paper):. Although absolute values seem to exhibit a factor of 2 discrepancy with the experimental measurements presented in Figure 6a, the trend in the temperature dependence of the Seebeck coefficient is well reproduced in the simulations. In particular, the magnitude of the calculated Seebeck coefficient reaches its maximum at ~480 K before slowly decreasing with increasing temperature, in excellent agreement with the experiment.

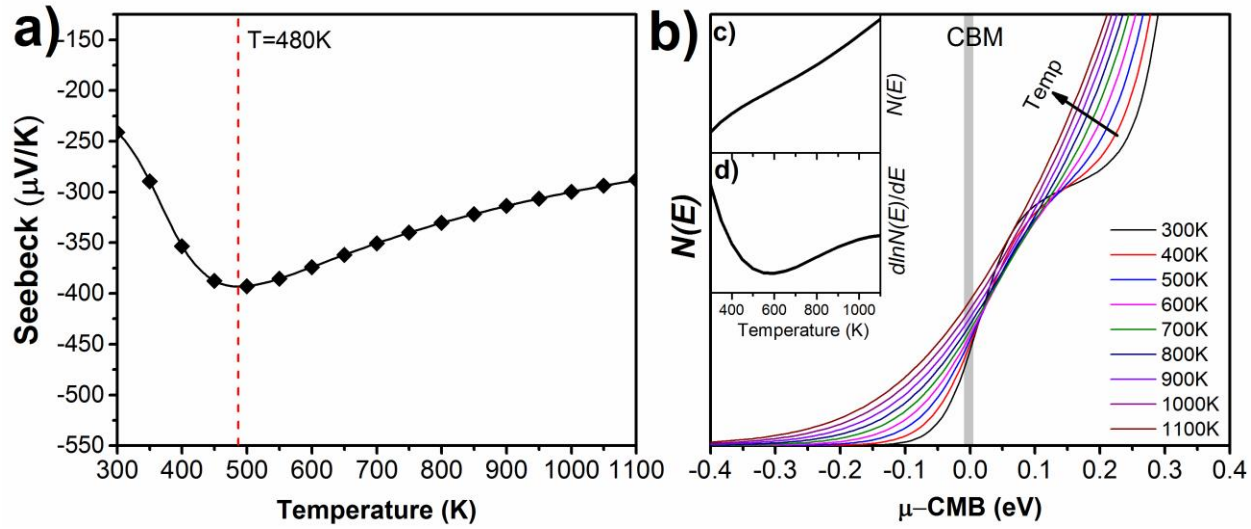

Figure 9: a) Calculated Seebeck coefficient as a function of temperature (results are averaged over all crystallographic directions). The red line indicates the temperature for which the Seebeck coefficient has the highest value; b) DOS as a function of chemical potential for various temperatures in the vicinity of the CBM; c) DOS and d) its logarithmic derivative as a function of temperature.

The temperature behaviour of the Seebeck coefficient is generally expressed *via* the Mott expression in Equation 2.[71]

$$S(T) = -\frac{\pi^2 k_B^2}{3|e|}\left(\frac{d\ln N(E)}{dE}\right)_{\mu} T \qquad (2)$$

where k_B is the Boltzmann constant, e the electron charge, $N(E)$ the DOS, μ the chemical potential and T the temperature. According to Equation 2, the Seebeck coefficient is directly related to the topology of the DOS and carrier diffusivity near the band edge. Figure 9b shows the evolution of the DOS with temperature in the vicinity of the conduction band minimum (CBM). The temperature-dependent blurring of the Fermi-Dirac statistics leads to the DOS at the CBM becoming smoother and gradually increasing as the temperature rises. At temperatures of around 500 K there is a slight change in the slope of the DOS that leads to a minimum of its logarithmic derivative (Figure 9b, inset). As a result the absolute value of the Seebeck coefficient increases at a temperature of ~500 K, as observed experimentally, and starts to decrease thereafter at the expense of a rise in electronic conductivity.

3.4 Tailoring LNO as a high efficiency thermoelectric

Electron doping

The temperature dependence of the transport coefficients is generally attributed to a combination of thermal generation of carriers and doping.[71] Having thoroughly investigated the evolution of the density of states in LNO as a function of temperature, in the following, a rigid-band model is used to simulate the effect of a change in electron doping concentration. This could in principle be achieved in LNO through chemical donor doping, taking advantage of its high vacancy content and structural similarities with STO. Note that this model assumes that a moderate level of doping does not change the shape of the band structure but only shifts the Fermi energy. The doping concentration dependence of the Seebeck coefficient calculated in this fashion for various temperatures is shown in Figure 10.

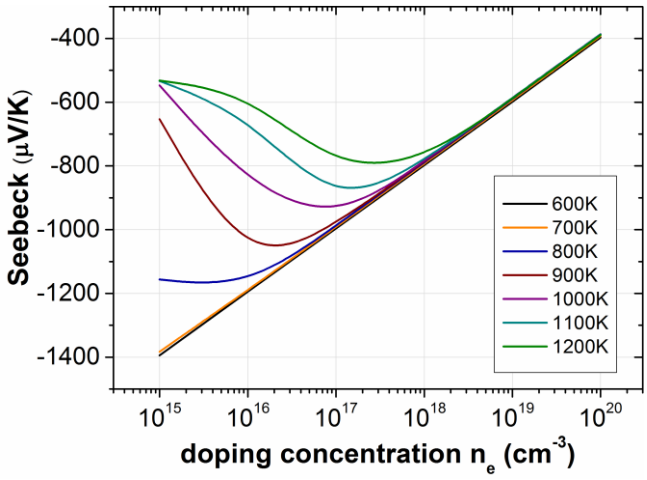

Figure 10: Calculated Seebeck coefficient dependence on the doping concentration for various temperatures, using a rigid-band model that assumes no shape change in the band structure, but only a shift in the Fermi energy due to the changing electron doping concentration.

The Seebeck coefficient curves as a function of temperature and carrier concentrations for the simulated electron doping within the rigid-band model shown in Figure 10 resemble the pattern observed in the undoped case shown in Figure 9a. The calculations show that for temperatures above 800 K there is an enhancement of the Seebeck coefficient up to electron doping level of 10^{18} cm^{-3}. This coincides with the change from ionic to electronic conduction above 800 K

observed experimentally.[60] For temperatures below 800 K, the Seebeck coefficient behaves almost identically for all temperatures, with a linear decrease in magnitude as the carrier concentration increases.

The high value of the calculated Seebeck coefficients at high temperatures for doping concentrations of 10^{16}-10^{18} cm^{-3} can be explained by the band convergence effect,[72] which occurs due to thermal blurring of the energy bands *via* the Fermi-Dirac function. At high temperatures the two lowest conduction bands at the Γ-point and Z-point are allowed to overlap (k_BT=69 meV for T=800 K exceeds ΔE~35 meV) and contribute to the transport properties. Note that the properties calculated here correspond to perfect single crystals while experimental samples may contain different types of imperfections (such as impurities, grain boundaries, vacancies, point defects, *etc.*) that may strongly affect TE properties, in particular electron transport properties. Therefore, due to the complexity of the phenomena that should be taken into account, obtaining a full quantitative agreement between calculated and experimental electronic transport properties is challenging. However, *ab initio* modelling can still inform the experiments and provide trends to explain the complex experimental behaviour of materials.

Table 2 provides selected values for the Seebeck coefficients at certain carrier concentrations and temperatures to highlight the fact that the coefficient is maximised for significantly different doping concentrations at different temperatures. This suggests that in order to maximise the thermopower ($S^2\sigma$) of LNO in a wider temperature range, the material needs to possess significantly different doping concentrations at different temperatures. This could in principle be achieved by a functional grading of the dopant concentration *i.e.* using lower dopant concentration on the cold side of the TE device, and progressively increasing the dopant concentration towards the hot side. However, such an approach may present technological challenges due to diffusion effects and dopant solubility dependence with temperature. Finally, our electronic transport properties calculations also support that the injection of electronic carriers may increase electrical conductivity (Figure S10). However, as discussed previously one has to be careful, that beyond a certain carrier concentration, electron doping will affect the Seebeck coefficient to an opposite extent compared to the electrical conductivity.

Table 2: Calculated maximum Seebeck coefficient for given temperature and electron doping concentration.

Seebeck (μV/K)	Temperature (K)	Doping Concentration (e/cm^{-3})
-1161	800 K	$4.9x10^{15}$
-1047	900 K	$1.8x10^{16}$
-929	1000 K	$7.7x10^{16}$
-868	1100 K	$1.4x10^{17}$
-789	1200 K	$2.8x10^{17}$

Vacancies and O bonding environment

The atomic-resolution chemical and structural study of LNO using STEM-EELS suggests a possible pathway to achieve the required doping, through the control of A_1-site cation/vacancy clustering. Due to a requirement of charge neutrality, the local cation vacancy clustering observed experimentally may result in the presence of associated O vacancies. Using PBE+*U* we have calculated the formation energy of a neutral oxygen vacancy to be 1.41 eV for $La_{1/3}NbO_{3-\delta}$ (δ=0.02). As noted previously, oxygen vacancies formed in this fashion lead to a partial reduction of Nb states, which can be seen by the population of the conduction bands of Nb character in Figure 11a. Interestingly, these states have a ferromagnetic ordering and are delocalized over Nb $4d_{xy}$ bands on every other Nb plane as shown in Figure 11b.

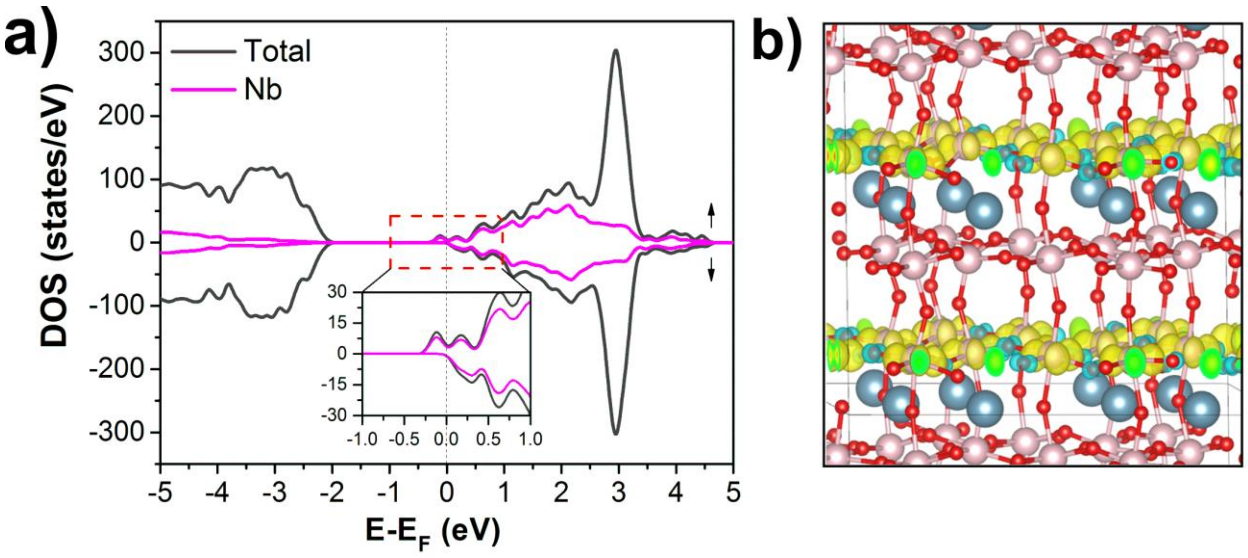

Figure 11: a) DOS and b) spin density iso surface of $1.4 \cdot 10^{-3}$ $\mu_B/Å^3$ for oxygen deficient $La_{1/3}NbO_{3-\delta}$ (δ=0.02). An approximate position of the oxygen vacant site is shown by a dashed circle.

Vacancies and thermal conductivity

The most attractive property of LNO as a TE candidate material system is arguably its relatively low thermal conductivity (Figure 6b). Calculations of the thermal conductivity along different lattice directions provide evidence for this. The averaged value over all crystallographic directions is found to be 2.3 W/mK for the range of temperatures considered, a theoretical prediction again fully supported by measured experimental values. Interestingly, the lattice thermal conductivity exhibits a weak anisotropy with crystallographic direction, being relatively suppressed along the *c*-axis (Figure 12).

Further controlling or hindering the non-uniform distribution of vacancies in the A_1-site through synthesis or processing steps could therefore exacerbate this transport anisotropy and thus further suppress the thermal conductivity along one of the main crystal axes.

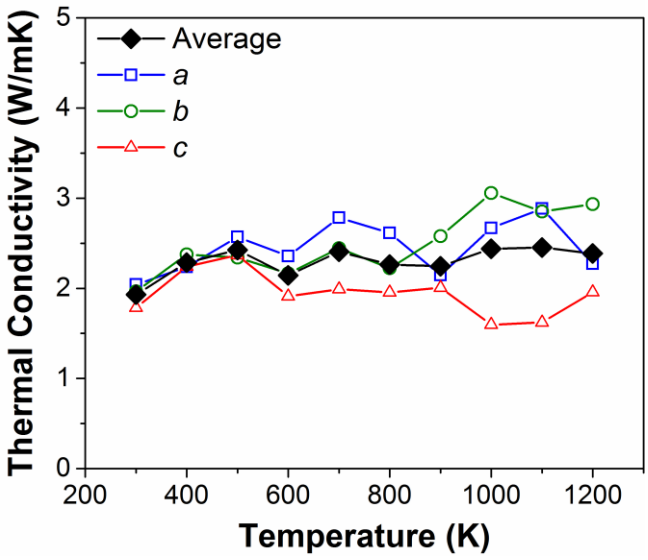

Figure 12: Calculated thermal conductivity along the different lattice directions.

4. Conclusion

We have combined experimental and computational techniques to investigate the chemical and electronic structure as well as the thermoelectric transport properties of the A-site deficient $La_{1/3}NbO_3$ (LNO) perovskite. The material is shown to possess a high Seebeck coefficient along with a low, temperature-stable, thermal conductivity. *Ab initio* calculations support the experimental measurements and reveal that LNO possesses a desirable band-structure for *n*-type thermoelectric materials. Interestingly, it exhibits a weak anisotropy of the lattice thermal conductivity with crystallographic direction. This places LNO among the best thermoelectric oxide materials in terms of (low) thermal conductivity.[1]

An increase of electrical conductivity is required to improve the thermoelectric performance of LNO. Our calculations show that with an appropriate electron doping and pertinent choice of operating temperature the electronic transport properties can be enhanced, making $La_{1/3}NbO_3$ a promising thermoelectric material for high temperature applications. This can for instance can achieved *by* reducing the valence of the B-site element, either employing a thermal treatment in a reducing atmosphere (for instance during the sintering stage or as a separate post-treatment), an approach similar to that used for other TE oxides.[15,64] Perhaps the most promising approach is the partial substitution of both A and B sites with elements of different valance state, for instance

Ca and Sr for the A- site and Ti and Mo for the B-site, respectively, before applying thermal treatment [15] Calculations also suggest that a functional grading of the material's electronic doping profile would widen its working temperature. It would also allow for band engineering, aimed to tune the density of states by exploiting the temperature dependence of the effective band degeneracy through a band convergence behaviour predicted to occur by our calculations. Finally control of vacancy clustering in the material, specifically designed to enhance thermal conduction anisotropy and further influence the electronic structure, should be eminently possible using synthesis and processing techniques that have proved very successful in parent systems[10].

Footnotes

[i] For simplicity, the HAADF intensity dependence is considered to be proportional the square modulus of the atomic number Z, i.e. $I \propto Z^2$. Multi-slice HAADF image simulations, corresponding to the experimental conditions are included in the Supplementary Information provided. (from page 10)

Acknowledgments

The authors gratefully acknowledge the support and the provision of funding from EPSRC for this work through grans EP/H043462, EP/I036230/1, EP/L014068/1, EP/L017695/1, EP/I03601X/1 and EP/K016288/1. The computational work made use of ARCHER, the UK's national HPC, via the Materials Chemistry Consortium funded by the EPSRC (EP/L000202) in addition to the HPC Balena at the University of Bath. SuperSTEM is the U.K. National Facility for Aberration Corrected STEM funded by EPSRC. Dr. Molinari acknowledges the University of Huddersfield. All data supporting this study are openly available from the University of Manchester data archive at DOI xxxx.

Supporting Information

Additional microscopy and structural data; XRD structural data, HAADF image simulations, EELS measurements. Additional computational details.

References

(1) Koumoto, K.; Wang, Y.; Zhang, R.; Kosuga, A.; Funahashi, R. Oxide Thermoelectric Materials: A Nanostructuring Approach. *Annu. Rev. Mater. Res.* **2010**, *40*, 363–394 DOI: 10.1146/annurev-matsci-070909-104521.

(2) Yeandel, S. R.; Molinari, M.; Parker, S. C. Nanostructuring Perovskite Oxides: The Impact of $SrTiO_3$ Nanocube 3D Self-Assembly on Thermal Conductivity. *RSC Adv.* **2016**, *6*, 114069–114077 DOI: 10.1039/C6RA23887D.

(3) Azough, F.; Freer, R.; Yeandel, S. R.; Baran, J. D.; Molinari, M.; Parker, S. C.; Guilmeau, E.; Kepaptsoglou, D.; Ramasse, Q.; Knox, A.; Gregory, D.; Paul, D.; Paul, M.; Montecucco, A.; Siviter, J.; Mullen, P.; Li, W.; Han, G.; Man, E. A.; Baig, H.; Mallick, T.; Sellami, N.; Min, G.; Sweet, T. $Ba_{6-3x}Nd_{8+2x}Ti_{18}O_{54}$ Tungsten Bronze: A New High-Temperature N-Type Oxide Thermoelectric. *J. Electron. Mater.* **2016**, *45*, 1894–1899 DOI: 10.1007/s11664-015-4275-6.

(4) Azough, F.; Cernik, R. J.; Schaffer, B.; Kepaptsoglou, D.; Ramasse, Q. M.; Bigatti, M.; Ali, A.; MacLaren, I.; Barthel, J.; Molinari, M.; Baran, J. D.; Parker, S. C.; Freer, R. Tungsten Bronze Barium Neodymium Titanate ($Ba_{6-3n}Nd_{8+2n}Ti_{18}O_{54}$): An Intrinsic Nanostructured Material and Its Defect Distribution. *Inorg. Chem.* **2016** DOI: 10.1021/acs.inorgchem.5b02594.

(5) Ohta, H.; Sugiura, K.; Koumoto, K. Recent Progress in Oxide Thermoelectric Materials: P-Type $Ca_3Co_4O_9$ and N-Type $SrTiO_3$. *Inorg. Chem.* **2008**, *47*, 8429–8436 DOI: 10.1021/ic800644x.

(6) Ohta, H.; Kim, S.; Mune, Y.; Mizoguchi, T.; Nomura, K.; Ohta, S.; Nomura, T.; Nakanishi, Y.; Ikuhara, Y.; Hirano, M.; Hosono, H.; Koumoto, K. Giant Thermoelectric Seebeck Coefficient of a Two-Dimensional Electron Gas in $SrTiO_3$. *Nat Mater* **2007**, *6*, 129–134.

(7) Srivastava, D.; Norman, C.; Azough, F.; Schäfer, M. C.; Guilmeau, E.; Kepaptsoglou, D.; Ramasse, Q. M.; Nicotra, G.; Freer, R. Tuning the Thermoelectric Properties of A-Site Deficient $SrTiO_3$ Ceramics by Vacancies and Carrier Concentration. *Phys. Chem. Chem. Phys.* **2016**, *18*, 26475–26486 DOI: 10.1039/C6CP05523K.

(8) Muta, H.; Kurosaki, K.; Yamanaka, S. Thermoelectric Properties of Rare Earth Doped $SrTiO_3$. *J. Alloys Compd.* **2003**, *350*, 292–295 DOI: 10.1016/S0925-8388(02)00972-6.

(9) Janotti, A.; Jalan, B.; Stemmer, S.; Van de Walle, C. G. Effects of Doping on the Lattice Parameter of $SrTiO_3$. *Appl. Phys. Lett.* **2012**, *100*, 262104 DOI: 10.1063/1.4730998.

(10) Jackson, S.; Azough, F.; Freer, R. Neodymium-Strontium Titanate: A New Ceramic for an Old Problem. *J. Electron. Mater.* **2014**, *43*, 2331–2336 DOI: 10.1007/s11664-014-3058-9.

(11) Kepaptsoglou, D.; Azough, F.; Hernandez-Maldonado, D.; Freer, R.; Ramasse, Q. Detection of Oxygen Sub-Lattice Ordering in A-Site Deficient Perovskites through Monochromated Core-Loss EELS Mapping. *Microsc. Microanal.* **2016**, *22*, 262–263 DOI: 10.1017/S1431927616002166.

(12) Azough, F.; Kepaptsoglou, D. .; Srivastava, D.; Ramasse, Q. M.; Freer, R. Crystal Structure, Cation Occupancy and Vacancy Ordering in Thermoelectric $_{(1-x)}SrTiO_{3-x}La_{1/3}NbO_3$: A STEM-EELS Study. *Microsc. Microanal.* **2014**, *20*, 1958–1959 DOI: 10.1017/S1431927614011520.

(13) Popuri, S. R.; Scott, A. J. M.; Downie, R. A.; Hall, M. A.; Suard, E.; Decourt, R.; Pollet, M.; Bos, J.-W. G. Glass-like Thermal Conductivity in $SrTiO_3$ Thermoelectrics Induced by A-Site Vacancies. *RSC Adv.* **2014**, *4*, 33720–33723 DOI: 10.1039/C4RA06871H.

(14) Ångqvist, M.; Lindroth, D. O.; Erhart, P. Optimization of the Thermoelectric Power Factor: Coupling between Chemical Order and Transport Properties. *Chem. Mater.* **2016**, *28*, 6877–6885 DOI: 10.1021/acs.chemmater.6b02117.

(15) Srivastava, D.; Azough, F.; Molinari, M.; Parker, S. C.; Freer, R. High-Temperature Thermoelectric Properties of $_{(1-X)}SrTiO_{3-(X)}La_{1/3}NbO_3$ Ceramic Solid Solution. *J. Electron. Mater.* **2015**, *44*, 1803–1808 DOI: 10.1007/s11664-014-3560-0.

(16) Kikuchi, A.; Okinaka, N.; Akiyama, T. A Large Thermoelectric Figure of Merit of La-Doped $SrTiO_3$ Prepared by Combustion Synthesis with Post-Spark Plasma Sintering. *Scr. Mater.* **2010**, *63*, 407–410 DOI: 10.1016/j.scriptamat.2010.04.041.

(17) Lu, Z.; Zhang, H.; Lei, W.; Sinclair, D. C.; Reaney, I. M. High-Figure-of-Merit

Thermoelectric La-Doped A-Site-Deficient $SrTiO_3$ Ceramics. *Chem. Mater.* **2016**, *28*, 925–935 DOI: 10.1021/acs.chemmater.5b04616.

(18) Zhang, B.; Wang, J.; Zou, T.; Zhang, S.; Yaer, X.; Ding, N.; Liu, C.; Miao, L.; Li, Y.; Wu, Y. High Thermoelectric Performance of Nb-Doped $SrTiO_3$ Bulk Materials with Different Doping Levels. *J. Mater. Chem. C* **2015**, *3*, 11406–11411 DOI: 10.1039/C5TC02016F.

(19) Wang, N.; Chen, H.; He, H.; Norimatsu, W.; Kusunoki, M.; Koumoto, K. Enhanced Thermoelectric Performance of Nb-Doped $SrTiO_3$ by Nano-Inclusion with Low Thermal Conductivity. *Sci. Rep.* **2013**, *3*, 3449 DOI: 10.1038/srep03449.

(20) Wiendlocha, B.; Kutorasinski, K.; Kaprzyk, S.; Tobola, J. Recent Progress in Calculations of Electronic and Transport Properties of Disordered Thermoelectric Materials. *Scr. Mater.* **2016**, *111*, 33–38 DOI: 10.1016/j.scriptamat.2015.04.014.

(21) Krivanek, O. L.; Lovejoy, T. C.; Murfitt, M. F.; Skone, G.; Batson, P. E.; Dellby, N. Towards Sub-10 meV Energy Resolution STEM-EELS. *J. Phys. Conf. Ser.* **2014**, *522*, 12023 DOI: 10.1088/1742-6596/522/1/012023.

(22) Lucas, G.; Burdet, P.; Cantoni, M.; Hébert, C. Multivariate Statistical Analysis as a Tool for the Segmentation of 3D Spectral Data. *Micron* **2013**, *52–53*, 49–56 DOI: 10.1016/j.micron.2013.08.005.

(23) Jones, L.; Yang, H.; Pennycook, T. J.; Marshall, M. S. J.; Van Aert, S.; Browning, N. D.; Castell, M. R.; Nellist, P. D. Smart Align—a New Tool for Robust Non-Rigid Registration of Scanning Microscope Data. *Adv. Struct. Chem. Imaging* **2015**, *1*, 8 DOI: 10.1186/s40679-015-0008-4.

(24) HREM Research. SmartAlign for Digital Micrograph. 2016, p https://www.hremresearch.com.

(25) Jones, L.; Nellist, P. D. Identifying and Correcting Scan Noise and Drift in the Scanning Transmission Electron Microscope. *Microsc. Microanal.* **2013**, *19*, 1050–1060 DOI: DOI: 10.1017/S1431927613001402.

(26) HREM Research. Jitterbug for Digital Micrograph. p https://www.hremresearch.com/.

(27) P. A. Stadelmann. JEMS. 2016, p http://www.jems-ch/.

(28) Barthel, J. Dr. Probe- STEM Simulation Software. 2016, p http://www.er-org/barthel/drprobe.

(29) Carrillo, L.; Villafuerte-Castrejón, M. E.; González, G.; Sansores, L. E.; Bucio, L.; Duque, J.; Pomés, R. Superstructure Determination of the Perovskite β $La_{0.33}NbO_3$. *J. Mater. Sci.* **2000**, *35*, 3047–3052 DOI: 10.1023/A:1004863715548.

(30) Blöchl, P. E. Projector Augmented-Wave Method. *Phys. Rev. B* **1994**, *50*, 17953–17979 DOI: 10.1103/PhysRevB.50.17953.

(31) Kresse, G.; Hafner, J. Ab Initio Molecular Dynamics for Liquid Metals. *Phys. Rev. B* **1993**, *47*, 558–561 DOI: 10.1103/PhysRevB.47.558.

(32) Kresse, G.; Hafner, J. Ab Initio Molecular-Dynamics Simulation of the Liquid-Metal–amorphous-Semiconductor Transition in Germanium. *Phys. Rev. B* **1994**, *49*, 14251–14269 DOI: 10.1103/PhysRevB.49.14251.

(33) Kresse, G.; Furthmüller, J. Efficiency of Ab-Initio Total Energy Calculations for Metals and Semiconductors Using a Plane-Wave Basis Set. *Comput. Mater. Sci.* **1996**, *6*, 15–50 DOI: 10.1016/0927-0256(96)00008-0.

(34) Perdew, J. P.; Burke, K.; Ernzerhof, M. Generalized Gradient Approximation Made Simple. *Phys. Rev. Lett.* **1996**, *77*, 3865–3868 DOI: 10.1103/PhysRevLett.77.3865.

(35) Dudarev, S. L.; Botton, G. A.; Savrasov, S. Y.; Humphreys, C. J.; Sutton, A. P. Electron-Energy-Loss Spectra and the Structural Stability of Nickel Oxide: An LSDA+U Study. *Phys. Rev. B* **1998**, *57*, 1505–1509 DOI: 10.1103/PhysRevB.57.1505.

(36) Kröger, F. A.; Vink, H. J. Relations between the Concentrations of Imperfections in Crystalline Solids; Physics, F. S. and D. T. B. T.-S. S., Ed.; Academic Press, 1956; Vol. Volume 3, pp 307–435.

(37) Buckeridge, J.; Taylor, F. H.; Catlow, C. R. A. Efficient and Accurate Approach to Modeling the Microstructure and Defect Properties of $LaCo_3$. *Phys. Rev. B* **2016**, *93*, 155123 DOI: 10.1103/PhysRevB.93.155123.

(38) Madsen, G. K. H.; Singh, D. J. BoltzTraP. A Code for Calculating Band-Structure Dependent Quantities. *Comput. Phys. Commun.* **2006**, *175*, 67–71 DOI: 10.1016/j.cpc.2006.03.007.

(39) Molinari, M.; Tompsett, D. A.; Parker, S. C.; Azough, F.; Freer, R. Structural, Electronic and Thermoelectric Behaviour of $CaMnO_3$ and $CaMnOCaMnO_{3-\Delta}$. *J. Mater. Chem. A* **2014**, *2*, 14109–14117 DOI: 10.1039/C4TA01514B.

(40) Baran, J. D.; Kepaptsoglou, D.; Molinari, M.; Kulwongwit, N.; Azough, F.; Freer, R.; Ramasse, Q. M.; Parker, S. C. Role of Structure and Defect Chemistry in High-Performance Thermoelectric Bismuth Strontium Cobalt Oxides. *Chem. Mater.* **2016**, *28*, 7470–7478 DOI: 10.1021/acs.chemmater.6b03200.

(41) Baran, J. D.; Molinari, M.; Kulwongwit, N.; Azough, F.; Freer, R.; Kepaptsoglou, D.; Ramasse, Q. M.; Parker, S. C. Tuning Thermoelectric Properties of Misfit Layered Cobaltites by Chemically Induced Strain. *J. Phys. Chem. C* **2015**, *119*, 21818–21827 DOI: 10.1021/acs.jpcc.5b05583.

(42) Plimpton, S. Fast Parallel Algorithms for Short-Range Molecular Dynamics. *J. Comput. Phys.* **1995**, *117*, 1–19 DOI: 10.1006/jcph.1995.1039.

(43) Canepa, P. New Insights on Iron and Lead-Based Materials beyond Density Functional Theory, University of Kent, 2012.

(44) Green, M. S. Markoff Random Processes and the Statistical Mechanics of Time-Dependent Phenomena. II. Irreversible Processes in Fluids. *J. Chem. Phys.* **1954**, *22*, 398–413 DOI: 10.1063/1.1740082.

(45) Kubo, R. Statistical-Mechanical Theory of Irreversible Processes. I. General Theory and Simple Applications to Magnetic and Conduction Problems. *J. Phys. Soc. Japan* **1957**, *12*, 570–586 DOI: 10.1143/JPSJ.12.570.

(46) Srivastava, D.; Azough, F.; Freer, R.; Combe, E.; Funahashi, R.; Kepaptsoglou, D. M.; Ramasse, Q. M.; Molinari, M.; Yeandel, S. R.; Baran, J. D.; Parker, S. C. Crystal Structure and Thermoelectric Properties of Sr–Mo Substituted CaMnO 3 : A Combined Experimental and Computational Study. *J. Mater. Chem. C* **2015**, *3*, 12245–12259 DOI:

10.1039/C5TC02318A.

(47) Iyer, P. N.; Smith, A. J. Double Oxides Containing Niobium, Tantalum, or Protactinium. III. Systems Involving the Rare Earths. *Acta Crystallogr.* **1967**, *23*, 740–746 DOI: 10.1107/S0365110X67003639.

(48) George, A. M.; Virkar, A. N. Thermal Expansion of β-$LaNb_3O$<sub>9</>. *J. Phys. Chem. Solids* **1992**, *53*, 733–736 DOI: 10.1016/0022-3697(92)90215-Y.

(49) Kennedy, B. J.; Howard, C. J.; Kubota, Y.; Kato, K. Phase Transition Behaviour in the A-Site Deficient Perovskite Oxide $La_{1/3}TaO_3$. *J. Solid State Chem.* **2004**, *177*, 4552–4556 DOI: 10.1016/j.jssc.2004.08.047.

(50) Salak, A. N.; Vyshatko, N. P.; Khalyavin, D. D.; Prokhnenko, O.; Ferreira, V. M. Low-Temperature Structural and Dielectric Phenomena in $La_{1/3}NbO_3$ and $La_{1/3}Ta_3$: Comparative Study. *Appl. Phys. Lett.* **2008**, *93*, 162903 DOI: 10.1063/1.3006331.

(51) García-Martín, S.; Alario-Franco, M. A. Modulated Structure of $La_{1/3-x}Li_{3x}NbO_3$ $0 \leq x \leq 0.06$ Perovskite-Related Materials. *J. Solid State Chem.* **1999**, *148*, 93–99 DOI: 10.1006/jssc.1999.8377.

(52) Robertson, A. D.; Martin, S. G.; Coats, A.; West, A. R. Phase Diagrams and Crystal Chemistry in the Li+ Ion Conducting Perovskites, $Li_{0.5-3x}RE_{0.5+x}TiO3$: Re=La, Nd. *J. Mater. Chem.* **1995**, *5*, 1405–1412 DOI: 10.1039/JM9950501405.

(53) Azough, F.; Kepaptsoglou, D.; Ramasse, Q. M.; Schaffer, B.; Freer, R. On the Origin of Nanochessboard Superlattices in A-Site-Deficient Ca-Stabilized $Nd_{2/3}TiO_3$. *Chem. Mater.* **2015**, *27*, 497–507 DOI: 10.1021/cm5036985.

(54) Abakumov, A. M.; Erni, R.; Tsirlin, A. A.; Rossell, M. D.; Batuk, D.; Nénert, G.; Tendeloo, G. Van. Frustrated Octahedral Tilting Distortion in the Incommensurately Modulated $Li_{3x}Nd_{2/3-x}TiO_3$ Perovskites. *Chem. Mater.* **2013**, *25*, 2670–2683 DOI: 10.1021/cm4012052.

(55) Zhu, Y.; Withers, R. L.; Bourgeois, L.; Dwyer, C.; Etheridge, J. Direct Mapping of Li-Enabled Octahedral Tilt Ordering and Associated Strain in Nanostructured Perovskites. *Nat. Mater.* **2015**, *14*, 1142–1149 DOI: 10.1038/nmat4390.

(56) Labeauu, M.; Grey, I. E.; Joubert, J. C.; Vincent, H.; Alario-Franco, M. A. Structural Studies on A -Cation-Deficient Perovskite-Related Phases. II. Microdomain Formation in $ThNb_4O_{12}$. *Acta Crystallogr. Sect. A* **1982**, *38*, 753–761 DOI: 10.1107/S0567739482001570.

(57) Lufaso, M. W.; Woodward, P. M. Jahn–Teller Distortions, Cation Ordering and Octahedral Tilting in Perovskites. *Acta Crystallogr. Sect. B Struct. Sci.* **2004**, *60*, 10–20 DOI: 10.1107/S0108768103026661.

(58) Wang, Y.; Sui, Y.; Wang, X.; Su, W.; Liu, X.; Fan, H. J. Thermal Conductivity of Electron-Doped $CaMnO_3$ Perovskites: Local Lattice Distortions and Optical Phonon Thermal Excitation. *Acta Mater.* **2010**, *58*, 6306–6316 DOI: 10.1016/j.actamat.2010.07.052.

(59) Voneshen, D. J.; Refson, K.; Borissenko, E.; Krisch, M.; Bosak, A.; Piovano, A.; Cemal, E.; Enderle, M.; Gutmann, M. J.; Hoesch, M.; Roger, M.; Gannon, L.; Boothroyd, A. T.; Uthayakumar, S.; Porter, D. G.; Goff, J. P. Suppression of Thermal Conductivity by Rattling Modes in Thermoelectric Sodium Cobaltate. *Nat. Mater.* **2013**, *12*, 1028–1032 DOI: 10.1038/nmat3739.

(60) George, A. M.; Virkar, A. N. Mixed Iono-Electronic Conduction in β-LaNb3O9. *J. Phys. Chem. Solids* **1988**, *49*, 743–751 DOI: 10.1016/0022-3697(88)90023-6.

(61) Tsubota, T.; Ohtaki, M.; Eguchi, K.; Arai, H. Thermoelectric Properties of Al-Doped ZnO as a Promising Oxide Material for High-Temperature Thermoelectric Conversion. *J. Mater. Chem.* **1997**, *7*, 85–90 DOI: 10.1039/a602506d.

(62) XU, G. High-Temperature Transport Properties of Nb and Ta Substituted $CaMnO_3$ System. *Solid State Ionics* **2004**, *171*, 147–151 DOI: 10.1016/S0167-2738(03)00108-5.

(63) Lee, S.; Yang, G.; Wilke, R. H. T.; Trolier-McKinstry, S.; Randall, C. A. Thermopower in Highly Reduced n-Type Ferroelectric and Related Perovskite Oxides and the Role of Heterogeneous Nonstoichiometry. *Phys. Rev. B* **2009**, *79*, 134110 DOI: 10.1103/PhysRevB.79.134110.

(64) Lee, S.; Wilke, R. H. T.; Trolier-McKinstry, S.; Zhang, S.; Randall, C. A. $Sr_xBa_{1-x}Nb_2O_{6-}$

$_{\Delta}$ Ferroelectric-Thermoelectrics: Crystal Anisotropy, Conduction Mechanism, and Power Factor. *Appl. Phys. Lett.* **2010**, *96*, 31910 DOI: 10.1063/1.3291563.

(65) McGuire, M. A.; Christianson, A. D.; Sefat, A. S.; Sales, B. C.; Lumsden, M. D.; Jin, R.; Payzant, E. A.; Mandrus, D.; Luan, Y.; Keppens, V.; Varadarajan, V.; Brill, J. W.; Hermann, R. P.; Sougrati, M. T.; Grandjean, F.; Long, G. J. Phase Transitions in LaFeAsO: Structural, Magnetic, Elastic, and Transport Properties, Heat Capacity and Mössbauer Spectra. *Phys. Rev. B* **2008**, *78*, 94517 DOI: 10.1103/PhysRevB.78.094517.

(66) Skelton, J. M.; Burton, L. A.; Parker, S. C.; Walsh, A.; Kim, C.-E.; Soon, A.; Buckeridge, J.; Sokol, A. A.; Catlow, C. R. A.; Togo, A.; Tanaka, I. Anharmonicity in the High-Temperature *Cmmm* Phase of SnSe: Soft Modes and Three-Phonon Interactions. *Phys. Rev. Lett.* **2016**, *117*, 75502 DOI: 10.1103/PhysRevLett.117.075502.

(67) Li, C. W.; Hong, J.; May, A. F.; Bansal, D.; Chi, S.; Hong, T.; Ehlers, G.; Delaire, O. Orbitally Driven Giant Phonon Anharmonicity in SnSe. *Nat. Phys.* **2015**, *11*, 1063–1069 DOI: 10.1038/nphys3492.

(68) Krukau, A. V.; Vydrov, O. A.; Izmaylov, A. F.; Scuseria, G. E. Influence of the Exchange Screening Parameter on the Performance of Screened Hybrid Functionals. *J. Chem. Phys.* **2006**, *125*, 224106 DOI: 10.1063/1.2404663.

(69) Cohen, A. J.; Mori-Sanchez, P.; Yang, W. Insights into Current Limitations of Density Functional Theory. *Science (80-.).* **2008**, *321*, 792–794 DOI: 10.1126/science.1158722.

(70) Inaguma, Y.; Muronoi, T.; Sano, K.; Tsuchiya, T.; Mori, Y.; Katsumata, T.; Mori, D. An Approach to Control of Band Gap Energy and Photoluminescence upon Band Gap Excitation in Pr^{3+}-Doped Perovskites $La_{1/3}MO_3$ (M = Nb, Ta): Pr^{3+}. *Inorg. Chem.* **2011**, *50*, 5389–5395 DOI: 10.1021/ic101955v.

(71) Maciá-Barber, E. *Thermoelectric Materials: Advances and Applications*, 1st ed.; Maciá-Barber, E., Ed.; Pan Stanford Publishing Pte. Ltd.: Signapore, 2015.

(72) Zaitsev, V. K.; Fedorov, M. I.; Gurieva, E. A.; Eremin, I. S.; Konstantinov, P. P.; Samunin, A. Y.; Vedernikov, M. V. Highly Effective Highly Effective $Mg_2Si_{1-x}Sn_x$ Thermoelectrics. *Phys. Rev. B* **2006**, *74*, 45207 DOI: 10.1103/PhysRevB.74.045207.

For Table of Contents Only

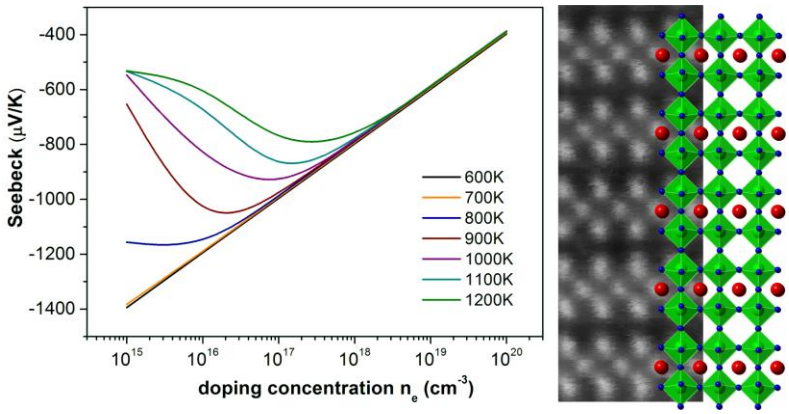

Table of Contents Synopsis

A combination of experimental and computational techniques has been employed to explore the crystal structure and thermoelectric properties of the A-site deficient $La_{1/3}NbO_3$. *Ab initio* simulations predict the system's thermoelectric properties change as a function of electron doping concentration, which atomic-scale characterisation suggests can be achieved by modifying the local structure. This offers a pathway to nanostructuring, into a promising and efficient thermoelectric material.